Inorganic Chemistry Communications 158 (2023) 111496

Contents lists available at ScienceDirect

Inorganic Chemistry Communications

journal homepage: www.elsevier.com/locate/inoche

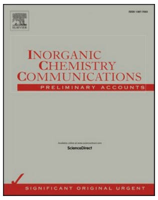

Short communication

Structure, DC electrical resistivity, and magnetic properties of Gd^{3+} substituted NiZnCo ferrites system

Tejeswararao Reddy [a], Sivasankar Reddy Akepati [a,*], V. Nagalakshmi [b], D. Jagadeeswara Rao [c,*], Ramakrishna Madaka [d]

[a] *Department of Physics, Vikram Simhapuri University College, Kavali, Andhra Pradesh, India*
[b] *Department of Chemistry, Ch. S. D. St. Theresa's College for Women (A), Eluru, A. P., India*
[c] *Department of Physics, S.V. Govt. Degree College, Parvathipuram, Andhra Pradesh, India*
[d] *Department of Physics, School of Sciences, Woxsen University, Hyderabad, Telangana, India*

ARTICLE INFO

Keywords:
Ferrite
Nanoparticles
XRD
DC resistivity
Magnetic parameters

ABSTRACT

Gd^{3+} substituted NiZnCo ferrite materials with the chemical formula $Ni_{0.4}Zn_{0.35}Co_{0.25}Fe_{2-x}Gd_xO_4$ (x = 0.0, 0.02, 0.04, 0.06, 0.08 and 0.1) were synthesized with the solid-state approach. We have concentrated more on the impact of ferrite synthesis on crystal structure, microstructure, and magnetoelectric characteristics. XRD shows the pure cubic spinel structure. Images taken with a SEM microscope supported the formation of nanoparticles. The sample's spinel structures were again validated with FTIR, confirming the existence of their functional group. Prepared samples' saturation magnetization, remanence, and coercivity were calculated using VSM data, which decreased with Gd^{3+} substitution. The metal-to-semiconductor transition was seen within the sample's DC resistivity study with respect to temperature.

1. Introduction

The cubic structure of spinel ferrites oxygen ions forms the face-center cubic structure of AB_2O_4. Each spinel cubic unit cell has 8 formula units. Additionally, each spinel cubic unit cell has 64 tetrahedral sites (A sites) and 32 octahedral sites (B sites) [1]. Therefore, the structure and formula of ferrite powders, which are subject to the techniques of manufacture, have a significant impact on their chemical and physical properties [2]. The properties of AB_2O_4 type nano ferrite groups can be altered by adding various types of cations to their tetrahedral and octahedral locations. By switching the types of cations, their structural, chemical, and physical properties can be systematically modified [3–5]. The microstructural and magnetic properties of the Spinel ferrite's were altered by the small-scale doping of rare earth ions [6]. High material resistivity makes NiZn ferrites work under high-frequency conditions [7]. Co^{2+} ions can increase the magneto-crystalline anisotropy (MCA) of NiZn ferrites, increasing the cut-off frequency [8]. Hichem Huili [9] has shown that $Co_{0.2}Ni_{0.3}Zn_{0.5}Fe_2O_4$ could be a more suitable alternative than NiZn ferrite for high-frequency technologies [9]. Recently, Al and Cr substitution efforts on the bulk ferrite characteristics of NiZnCo with lower sintering temperatures were reported [10]. In this case, the synthesis of Gd-substituted NiZnCo ferrite powders using a solid-state method has been considered. The synthesis route is beneficial and economical as it initially allows the use of cheap precursors, and it is also a straightforward preparation technique.

Moreover, low sintering temperatures can produce satisfactory and reactive ferrite powder [11–13]. The Rare Earth (RE) 4f and 3d electrons in magnetic cations are susceptible to interactions [14]. Distinct rare earth ions have significant impacts because of their unique properties. Hichem Huili investigated how Y and Gd additions affected the characteristics of $Co_{0.2}Ni_{0.3}Zn_{0.5}Fe_2O_4$ ferrite and discovered that the presence of rare earth metals enhances resistivity and resonance frequency while reducing the concentration of the Fe^{3+}/Fe^{2+} pair. They have reported increased sample Curie temperature after Y^{3+} doping; yet, by doping Gd^{3+}, they came up with decreased Curie temperature [15].

The present work showed that NiZnCo ferrite samples sintered using a ceramic route have shown improved magnetic properties than the previously reported works using the same synthesis methods. In this study, $Ni_{0.4}Zn_{0.35}Co_{0.25}Fe_{2-x}Gd_xO_4$ for x = 0.0, 0.02, 0.04,0.06, 0.08, and 0.1 ferrite materials were synthesized using ceramic method at sintering temperature of 1050 ^{0}C.

---

* Corresponding authors.
E-mail addresses: akepati77@gmail.com (S.R. Akepati), dasarijagadeesh@gmail.com (D.J. Rao).

https://doi.org/10.1016/j.inoche.2023.111496
Received 10 August 2023; Received in revised form 4 September 2023; Accepted 23 September 2023

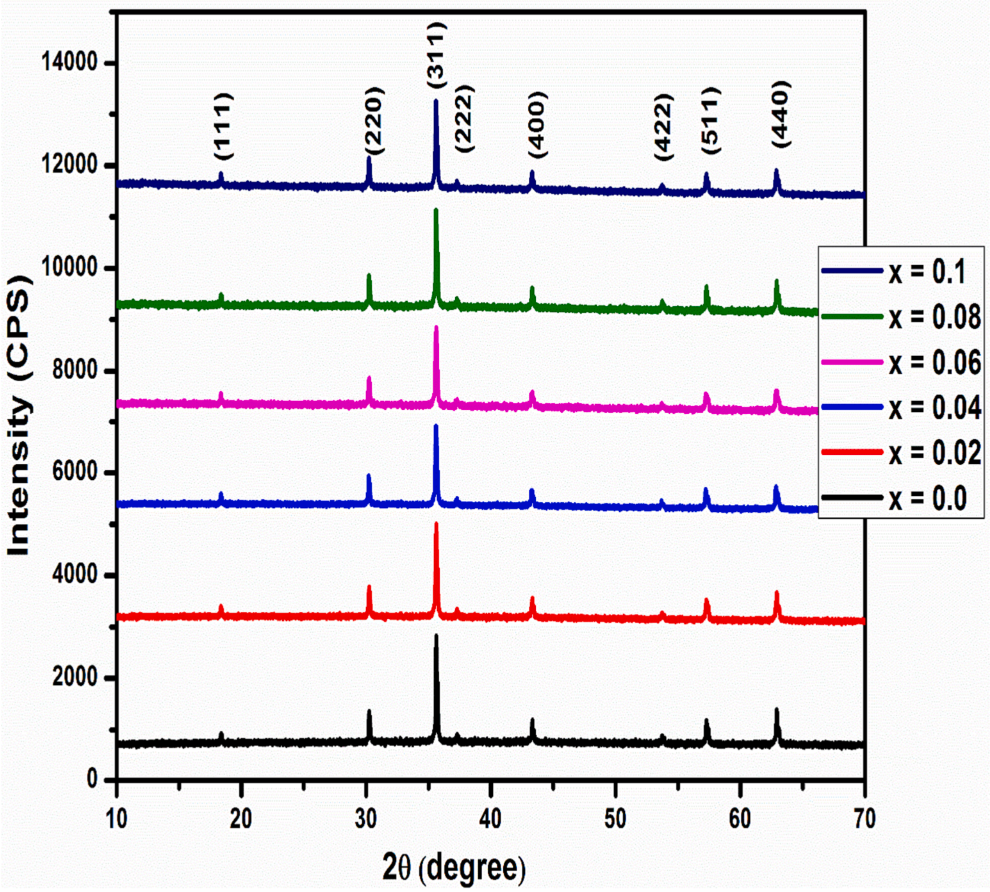

Fig. 1. XRD patterns of $Ni_{0.4}Zn_{0.35}Co_{0.25}Fe_{2-x}Gd_xO_4$.

Table1
Lattice parameters of $Ni_{0.4}Zn_{0.35}Co_{0.25}Fe_{2-x}Gd_xO_4$ ferrite system.

Compounds	Lattice constant (Å)	Molecular weight, M (g/mol)	X-ray density ρ_x(g/cm^3)	Bulk Density ρ_B(g/cm^3)	Porosity P (%)	Crystallite size (nm)
0.0	8.382	236.78	5.343	5.071	5.1	40.56
0.02	8.388	238.81	5.375	5.009	6.82	36.25
0.04	8.392	240.84	5.409	4.952	8.45	33.56
0.06	8.395	242.87	5.455	4.907	10.05	29.84
0.08	8.379	244.89	5.532	4.879	10.18	26.54
0.1	8.363	246.93	5.610	4.878	13.05	23.95

2. Experimental studies

$Ni_{0.4}Zn_{0.35}Co_{0.25}Fe_{2-x}Gd_xO_4$ is synthesized using the solid-state reaction method from the Merck limited analytical grade 98 % pure oxides of Nickel, Zinc, Cobalt, Gadolinium, and Iron as starting materials for x = 0.0, 0.02, 0.04,0.06, 0.08, and 0.1. Acetone is added to a mixture, which will be ground for 8 h to produce the intended sample for the next steps of the process. The product had 3 h of calcination at 900 °C, 3 h of grinding, 3 h of sintering at 1050 °C, and 3 h of grinding.

The structure was tested with an XRD (D8 ADVANCE) in the 2θ range of 20°–70°; SEM was used to examine the surface morphology of the synthesized powders; VERTEX70. FTIR spectrometer (Bruker) was used to record their functional group. The vibrating sample magnetometer (VSM) (BKT4500Z) was used for its magnetic properties. The two-probe approach was used to test the DC electrical resistance characteristics.

3. Results and discussion

3.1. XRD analysis

Fig. 1 displays the XRD patterns of samples of $Ni_{0.4}Zn_{0.35}Co_{0.25}Fe_{2-x}Gd_xO_4$ (x = 0.0, 0.02, 0.04,0.06, 0.08, and 0.1). All samples showed the main peaks (2 2 0), (3 3 1), 400, (4 2 2), (5 1 1), and 440, which match the NiZnCo ferrite (JCPDS data #74-2401) [16]. The XRD results showed the structure of the ferrites being cubic spinel [17]. The synthesized samples' crystallite sizes were determined with the help of the Debye-Scherrer formula [18],

$$D_{311} = \frac{0.9\lambda}{\beta cos\theta} \tag{1}$$

where λ, β, and θ have their usual meaning. The data are listed the Table 1. The Bragg equation [19] was used to determine the lattice constant (a) of Gd-doped ferrites, as shown in Table 1. Fig. 2 depicts how the lattice parameter and average crystallite size change as Gd^{3+} doping levels increase. The interplanar spacing d is obtained with the relation following Bragg's law,

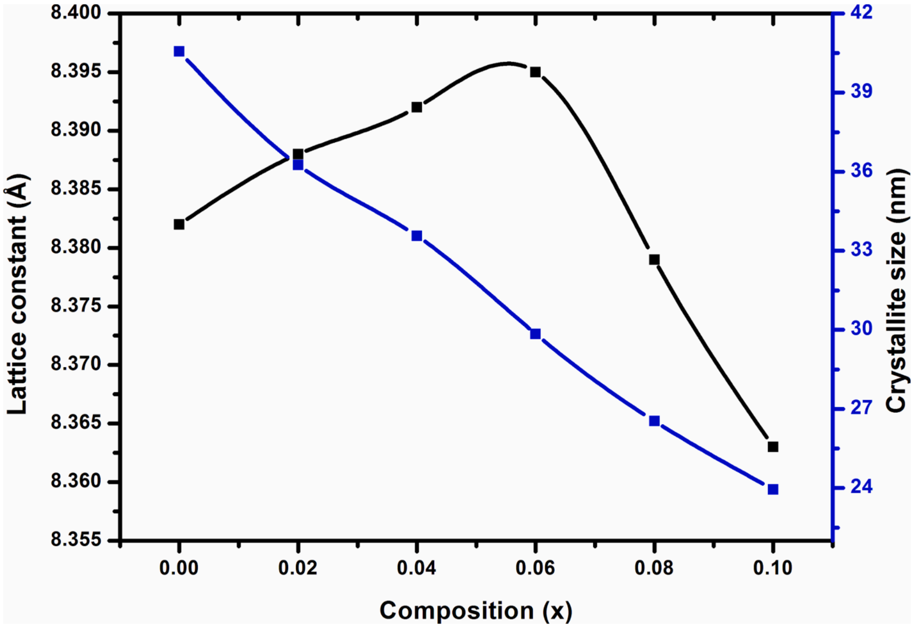

Fig. 2. Plot of Lattice constant (a) and Crystallite size (D) against composition (x) of $Ni_{0.4}Zn_{0.35}Co_{0.25}Fe_{2-x}Gd_xO_4$.

$$a = d_{hkl}\sqrt{h^2 + k^2 + l^2} \tag{2}$$

where a is the lattice parameter of the given *hkl* planes.

Table 1 shows no linear relationship between the increase in Gd^{3+} ions concentration and the lattice constant of synthesized ferrites. Because the radius of Gd^{3+} ions (0.938 Å) is greater than that of Fe^{3+} ions (0.645 Å), we observe the lattice constant expansion with lower dopant concentration. However, at a higher concentration of Gd^{3+}, it will mix with the Fe^{3+} and O^{2-} ions to create $GdFeO_3$ in the crystal structure. It is an impurity phase in the grain boundary and contributes to the extrusion of the ferrite grains. This impurity phase does not appear in the figure as it is very insignificant compared to the major peaks of the XRD pattern. The lattice almost doesn't change within a specific error range when the Gd^{3+} substitution content (x) is between 0.04 and 0.06. The modest rise in the lattice constant at x = 0.06 may be caused by the presence of the second phase $GdFeO_3$ at the material crystal's boundary, which differs from the growth trend of the ferrite primary term [20,22]. Moreover, there are clear and visible patterns of the XRD peaks showing the high crystalline nature and the polycrystalline states of the doped and undoped samples [23].

The sample's X-ray density, "ρ_x", can be determined using the formula below [14].

$$\rho_x = \frac{ZM}{N_A a^3} \tag{3}$$

The sublattice number in the spinel crystal lattice's unit cell is "Z = 8", and 'M' represents the sample's molecular weight at different doping doses. NA is the Avogadro constant, and its value is 6.02×10^{23} [16]. The bulk density is calculated using the formula below:

$$\rho_b = \frac{m}{\pi^2 RT} \tag{4}$$

Where 'm' stands for the sample's mass, 'R' for the sample's radius, and 't' for the sample's thickness.

The formula below calculates the samples' porosity '*P*' [19].

$$P = \left(1 - \frac{\rho_b}{\rho_x}\right) \times 100 \tag{5}$$

The bulk and X-ray densities are key factors in determining the characteristics of polycrystalline ferrites. Table 1 shows the impact of Gd^{3+} ions on the X-ray densities, bulk densities, and porosities. Inside the samples' crystal structures, pores form during the synthesis process. The composition, therefore, displays lower bulk densities than the predicted (X-ray) densities (Table 1). The Gd^{3+} contents have caused a slight declination in the X-ray densities. The intragranular porosity (Pintra), which is caused by pore volume by the grains and intergranular porosity (Pinter), which is due to the pore within the grain of samples, can be used to explain their porosities, P(%). The force that makes the grain boundaries develop over pores occurs during sintering due to the heat energy. The substance becomes denser as a result of the reduced pore volume. Since the synthesized ferrites' sintering temperature remained constant throughout the studies, the composition impacts on intragranular porosities were negligible. Intergranular porosities occur during sintering inside the ferrites due to irregular particles. The bulk densities and porosities of the compositions then follow an inverse relationship. Additionally, the pores allow for the passage of gaseous oxygen and the diffusion of cations in and around the pores. The examined ferrites' porosities rise with Gd^{3+} concentrations because there are more cation vacancies with less oxygen.

3.2. SEM analysis

The SEM pictures of the prepared $Ni_{0.4}Zn_{0.35}Co_{0.25}Fe_{2-x}Gd_xO_4$ (x = 0.0, 0.02, 0.04,0.06, 0.08, and 0.1) samples are displayed in Fig. 3. As the picture shows, the produced sample's grain has a spherical cubic form [21]. The particles appear to aggregate due to the sample's magnetic characteristics and the result of sintering at a high temperature [22]. According to the particle-size distribution plot, the samples exhibit homogeneous and thin particle sizes that vary from 1.7 to 1.98 μm. The findings demonstrate that distinct NiZnCo ferrite samples synthesized after adding Gd^{3+} have smaller grains than pure NiZnCo ferrite. This is because the Fe-O bond requires less energy to form than the Gd-O bond, which lowers the energy required for crystallization and results in smaller grains [24].

3.3. FTIR analysis

In the infrared spectrum, the typical absorption peaks of $Ni_{0.4}Zn_{0.35}Co_{0.25}Fe_{2-x}Gd_xO_4$ ferrites (x = 0.0, 0.02, 0.04,0.06, 0.08, and 0.1) were identified as in Fig. 4. The bands near 388–405 cm^{-1} (ν_2) and 580–610 cm^{-1} (ν_1) in spinel ferrite were caused by stretching between

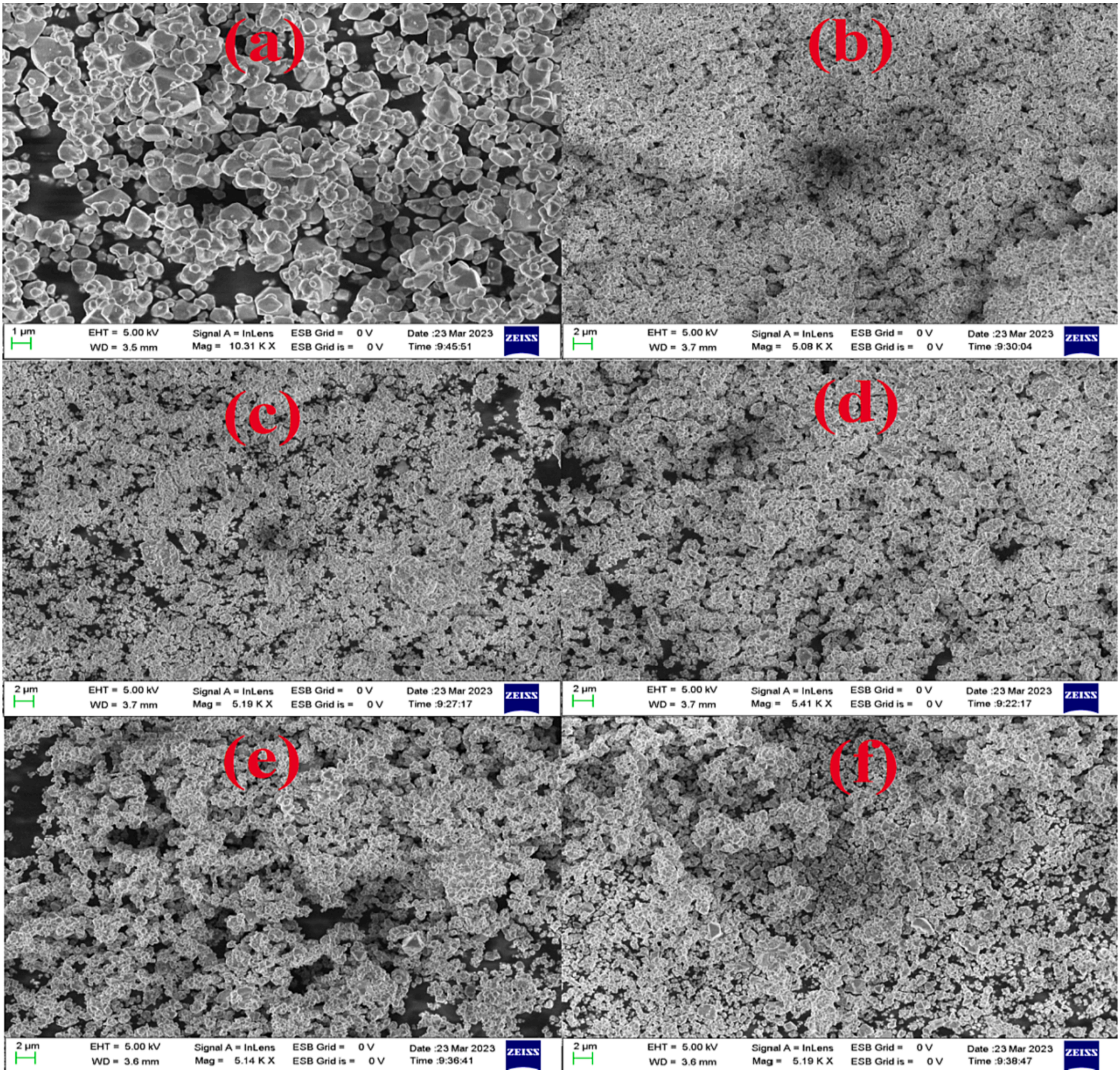

Fig. 3. SEM patterns of representative samples for $Ni_{0.4}Zn_{0.35}Co_{0.25}Fe_{2-x}Gd_xO_4$.

the metal ions of B-site, A-site, and the oxygen ion (M_{Oct}-O, M_{Tet}-O), respectively. The intensity and peak locations of the synthesized ferrites altered as the Gd^{3+} content rose compared to pure NiZnCo ferrite. The increase in Gd^{3+} replacing Fe^{3+} in octahedral site spreading v_2 has continuously altered Fe-O distances [25]. The introduction of Gd^{3+} ions perturbs the $Fe^{3+}cO_2$ link, causing variation in the absorption bands v_2 and v_1 for each B and A site, which are supported by the results of the earlier experiment [26]. Additionally, the bands of v_2 and v_1 showed weak absorption peaks at 388–405 cm^{-1} and 580–610 cm^{-1}, respectively, indicating Fe^{3+}–O_2 stretching vibration in the A site and Fe^{3+}/Gd^{3+}–O_2 in the B site [27] values tabulated in Table 2. At 2325–2351 cm^{-1}, a double band containing the sample's CH2-group stretching, symmetric and antisymmetric, is discernible. These bands are caused by the mixture of sucrose and metal nitrates generated [28]. As a result, this information shows that when we raise the sintering temperature, a pure crystalline phase is formed.

3.4. *VSM analysis*

The hysteresis loops of the $Ni_{0.4}Zn_{0.35}Co_{0.25}Fe_{2-x}Gd_xO_4$ ferrites ($x =$ 0.0, 0.02, 0.04,0.06, 0.08, and 0.1) are shown in Fig. 5. Table 3 provides the sample's saturation magnetization (Ms) and coercivity (Hc) with various Gd^{3+}. As common knowledge, Gd^{3+} has a more excellent magnetic moment (7μB) than Fe^{3+} (5μB) [29]. However, the synthesized sample's saturation magnetization (Ms) marginally decreases with x. This behavior was attributed to the fact that all rare earth ions are non-magnetic at ambient temperature due to the ordering of their magnetic moments being substantially lower [30]. According to P. Samoila, trivalent Gadolinium ions strongly prefer to occupy octahedral sites, and as the Gd^{3+} concentration rises, more octahedral ions experience anti-parallel moments [31]. As a result, the octahedral sites' net magnetic moment decreases. By computing the Yafet-Kittel angles, A. Kumar examined the spin configurations and discovered that the Y-K angles rise

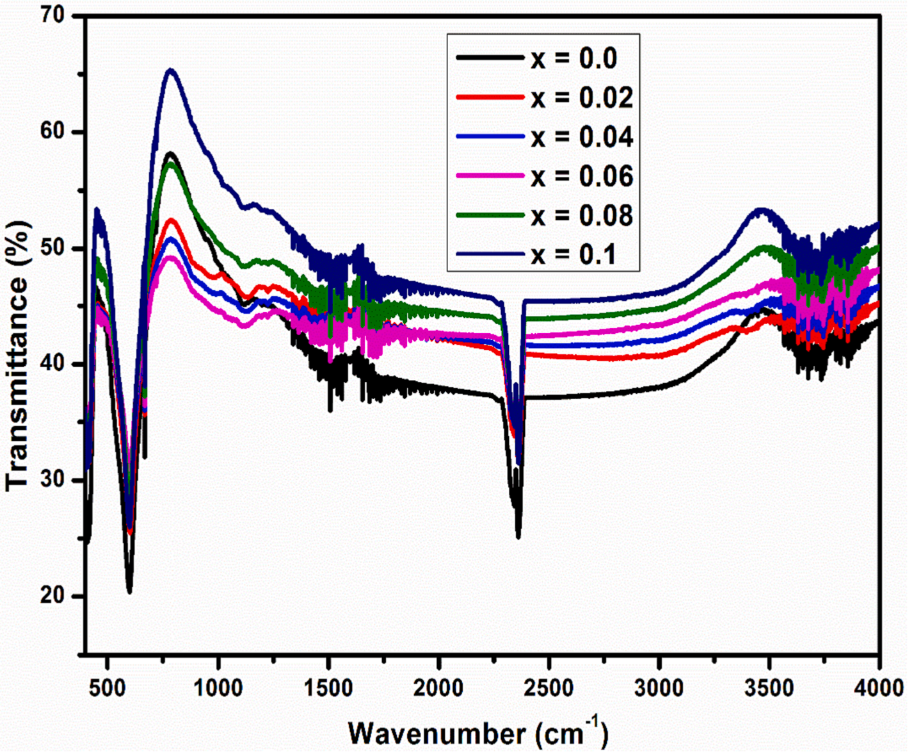

Fig. 4. FTIR spectra of synthesized $Ni_{0.4}Zn_{0.35}Co_{0.25}Fe_{2-x}Gd_xO_4$.

Table 2
Octahedral ($\upsilon2$) and tetrahedral ($\upsilon1$) absorption bands of $Ni_{0.4}Zn_{0.35}Co_{0.25}Fe_{2-x}Sm_xO_4$.

Composition (x)	Tetrahedral absorption band (υ_1)	Octahedral absorption band (υ_2)
0.0	580	388
0.02	585	392
0.04	592	396
0.06	596	397
0.08	599	402
0.1	610	405

with the concentration of Gd^{3+} [32]. The magnetic moment will decrease due to the change from collinear ferrimagnetism to random spin canting on B-sites [33]. Due to impurities, M_S will also decline as rare earth elements increase.

Acquiring the various magnetic properties, including coercivity, saturation magnetization, and remanence magnetization, is possible. Increased saturation magnetization can be seen in the pure ferrite sample, which aligns with previously reported results [34].

The most crucial ferrite material characteristic for memory devices is coercivity. In this study, we found that substituting Gd^{3+} ions in NiZnCo ferrite resulted in a decreasing and then increasing trend in the Hc values shown in Fig. 6. The significant drop in coercivity is brought on by a rise in magnetic crystalline anisotropy (MCA) at the anisotropic Fe^{2+} ion's tetrahedral position [35]. Additionally, non-magnetic atoms, grain size, flaws, stresses, surface impact, and other factors affect coercivity variations [36].

Additionally, the remanent magnetization (Mr), which was 29.89 emu/g, decreased in magnitude with the addition of dopants. Fig. 6 shows the saturation magnetization and coercivity of synthesized ferrite. The calculated aspect ratio (Mr/Ms) was less than 0.5, which caused the synthesized nanomaterials to form a multi-domain structure [23].

The magnetic moment (ηB) values for the synthesized nano ferrites were determined to be between 3.54 and 2.36 μ_B using the equation below, Table 3 lists the results [37].

$$\eta_B = \frac{M_s \times M.W}{5585} \tag{6}$$

Where Ms stands for saturation magnetization and M.W for the synthesized sample's molecular weight, the saturation magnetization (Ms) and the magnetic moment (η_B) of prepared samples are closely correlated; thus, as Ms declines, so does the value of η_B.

3.5. DC resistivity studies

DC electrical resistivity of $Ni_{0.4}Zn_{0.35}Co_{0.25}Fe_{2-x}Gd_xO_4$ ferrites (x = 0.0, 0.02, 0.04,0.06, 0.08, and 0.1) are shown in Fig. 7 showing increasing dc resistivity with concentration. The DC electrical resistivities were measured using two probe methods. The kind and composition of the cations used to replace the original ferrite structure, the synthesis method, and the sintering temperatures all play a role in DC electrical resistivity [37]. The preference of Gd^{3+} to occupy either A-sites (tetrahedral) or B-sites (octahedral) can explain this rise in resistivity. All three of the individuals tend to occupy B-sites [38]. Together with iron (Fe^{3+}) occupies a portion of both A and B sites. Shifting of Fe^{3+} ions from B to A sites with concentration reduces the electron hopping between Fe^{2+} and Fe^{3+}. These electron exchange interactions or A-B super-exchange interactions cause the high resistivity of ferrites. In this instance, Ni^{2+} fills the B-site, reducing the quantity of Co^{2+} and Zn^{3+} ions there, and Gd^{3+} fills the B-site in place of Fe^{3+}, reducing the amount of electron hopping between atoms of the same element in various valence states. The increase in Fe^{2+} at the A site leads to an increase in the hopping of electrons, which decreases resistivity for the sample [11]. The DC resistivity measurement between 368 K and 573 K shows the semiconducting nature [39]. This provides the sample's activation or hopping energy [40].

The activation energy is determined with the help of the Arrhenius plot [41] fitted linearly,

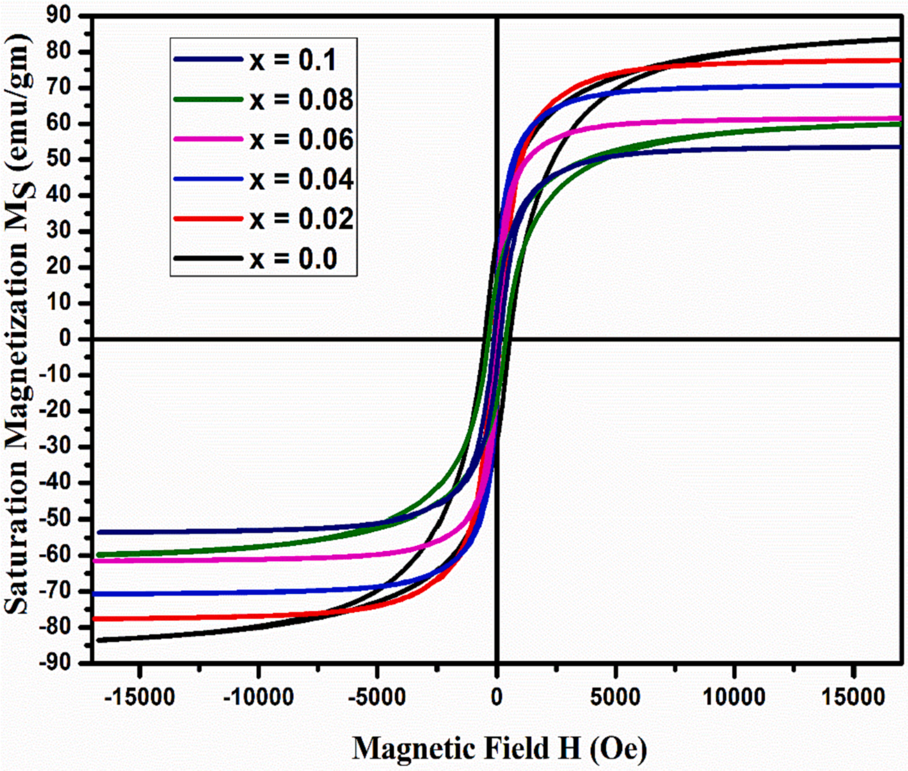

Fig. 5. Hysteresis loops of $Ni_{0.4}Zn_{0.35}Co_{0.25}Fe_{2-x}Gd_xO_4$.

Table 3

Magnetic Saturation, remnant magnetization, coercivity, aspect ratio, and magnetic moment values obtained from M–H curves for $Ni_{0.4}Zn_{0.35}Co_{0.25}Fe_{2-x}Gd_xO_4$.

Content (x)	Ms (emu/g)	Mr (emu/g)	Hc (Oe)	M_r/M_s	Magnetic moment (μ_B)
0.0	83.51	29.89	532.13	0.36	3.54
0.02	77.61	27.51	130.65	0.35	3.32
0.04	70.62	25.64	92.56	0.36	3.05
0.06	61.51	23.95	89.65	0.39	2.67
0.08	59.76	21.65	354.71	0.36	2.62
0.1	53.46	19.52	139.77	0.37	2.36

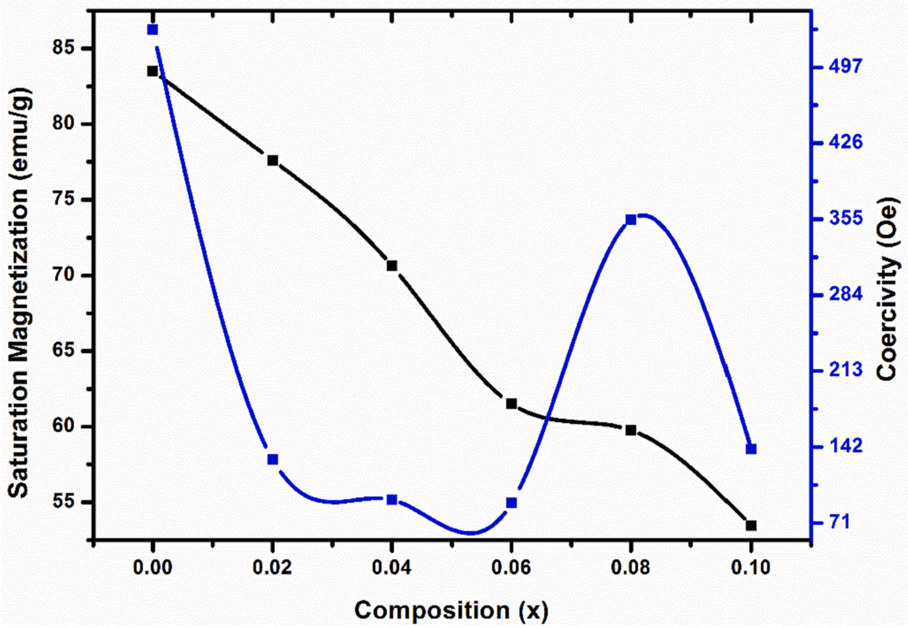

Fig. 6. Saturation magnetization and Coercivity values variation trends of $Ni_{0.4}Zn_{0.35}Co_{0.25}Fe_{2-x}Sm_xO_4$.

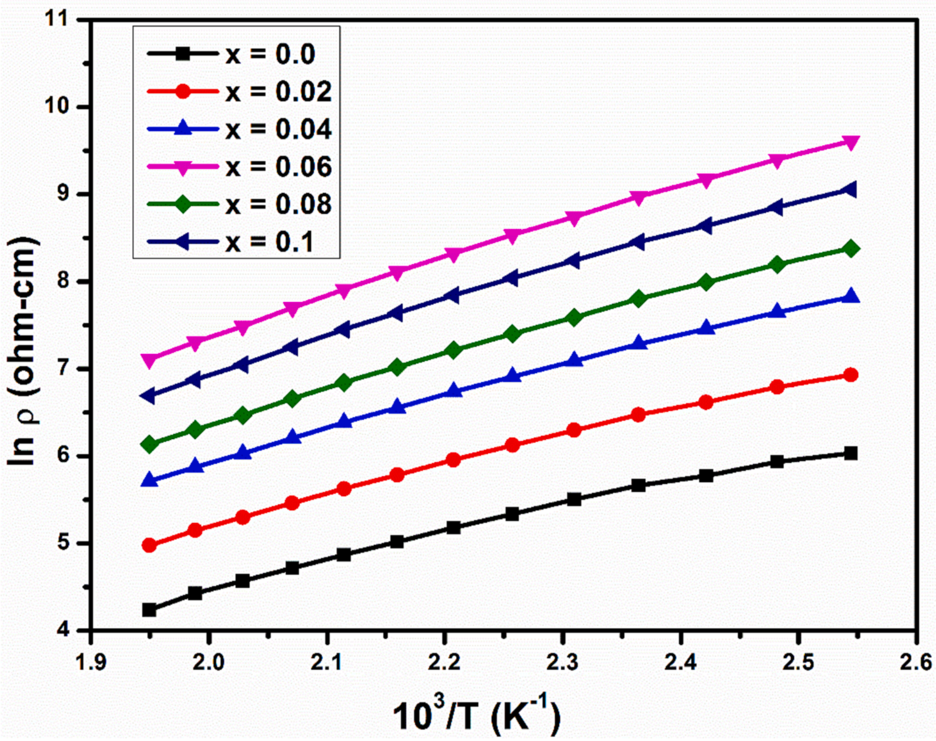

Fig. 7. DC resistivity as a function of temperature.

$$\rho = \rho_o e^{-\left(\frac{\Delta E}{KT}\right)} \tag{7}$$

Where ΔE is the activation energy, and K is the Boltzmann constant.

Fig. 8 displays the computed values of the ferrite nanoparticles' activation energies. The activation energies for all the examined samples are 0.35, 0.37, 0.45, 0.47, 0.52, and 0.55 eV, respectively. These low activation energy values indicate the electronic component of the materials' conductivity. According to the hopping mechanism described by Verwey and de Boer, electrons bounce between the multiple valence states of the same elements scattered over different sites. The estimated activation energy agrees with published data [42].

4. Conclusion

According to the XRD analysis of $Ni_{0.4}Zn_{0.35}Co_{0.25}Fe_{2\text{-}x}Gd_xO_4$ ferrites (x = 0.0, 0.02, 0.04,0.06, 0.08, and 0.1) ferrites, the solid-state reaction to prepare the spinel ferrites confirmed the pure cubic phase formation of the anticipated materials. By incorporating Gd^{3+} ions, it is seen that the lattice parameter first increases from 8.382 Å to 8.395 Å and then decreases to 8.363 Å, and the average crystallite size decreases from 40.56 to 23.95 nm. According to the morphological analysis, the sample exhibits a spherical cube shape, homogeneous particle size, and uniform texture. The cubic particles are layered and are visible in the SEM pictures. SEM examination supports the crystallinity and phase purity of the spinel ferrites. The two FT-IR absorption bands represent the spinel structure's tetrahedral A and octahedral B sites. The FTIR spectrum of the synthesized ferrites with two peaks at 388–405 cm^{-1} and 580–610 cm^{-1} shows the spinel phase formation related to the B and A sites, respectively. For Gd^{3+} substituted samples, the ferrite coercivity is reduced. Although Gd^{3+} presence reduces the saturation magnetization of the samples, the remanent magnetization decreases. Adding Gd^{3+} reduces the DC resistivity and, hence, the activation energy.

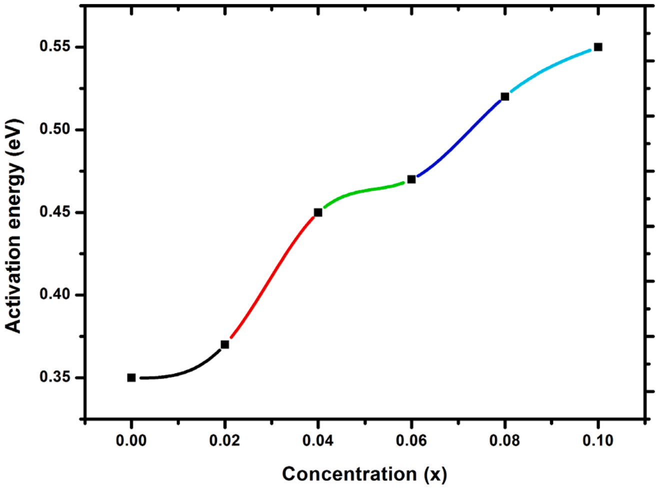

Fig. 8. Activation energies of the $Ni_{0.4}Zn_{0.35}Co_{0.25}Fe_{2\text{–}x}Gd_xO_4$.

Author contribution statements

All authors contributed to the study's conception and design. Tejeswararao Reddy, Sivasankar Reddy Akepati, V. Nagalakshmi, D. Jagadeeswara Rao, and Ramakrishna Madaka performed material preparation, data collection and analysis. D. Jagadeeswara Rao wrote the first draft of the manuscript, and all authors commented on previous versions. All authors read and approved the final manuscript.

CRediT authorship contribution statement

Tejeswararao Reddy: Conceptualization, Data curation, Investigation, Formal analysis, Methodology, Writing – original draft. **Sivasankar Reddy Akepati:** Formal analysis, Writing – review & editing. **V. Nagalakshmi:** Formal analysis, Writing – review & editing. **D. Jagadeeswara Rao:** Supervision, Formal analysis, Writing – review & editing. **Ramakrishna Madaka:** Supervision, Formal analysis, Writing – review & editing.

Declaration of Competing Interest

The authors declare that they have no known competing financial interests or personal relationships that could have appeared to influence the work reported in this paper.

Data availability

The data that has been used is confidential.

References

[1] E. Pervaiz, I.H. Gul, Low temperature synthesis and enhanced electrical properties by substitution of Al3+ and Cr3+ in Co–Ni nanoferrites, J. Magn. Magn. Mater. 343 (2013) 194–202.

[2] T. Wu, T. Zhan, F. Ding, Structural and magnetic properties of gadolinium substituted Mn0.6Zn0.4GdxFe2−xO4 (x= 0–0.1) spinel ferrite, J. Magn. Magn. Mater. 571 (2023), 170554.

[3] P. Vijayalaxmi, R. Mandala, S. Kunchalapalli, B. Suryanarayana, D.J. Rao, Y. Ramakrishna, Effect of Ce3+ on structural, morphological, DC electrical resistivity and magnetic studies of Co nano ferrites, Inorg. Chem. Commun. (2023), 110918.

[4] Z. Xueyun, Y. Dongsheng, Z. Liling, Improved cut-off frequency in Gd/La-doped NiZnCo ferrites, Mater. Sci. Eng. B 272 (2021), 115334.

[5] G.V. Priya, N. Murali, M.K. Raju, B. Krishan, D. Parajuli, P. Choppara, B.C. Sekhar, R. Verma, K.M. Batoo, P.L. Narayana, Influence of Cr3+ substituted NiZnCo nanoferrites: structural, magnetic and DC electrical resistivity properties, Appl. Phys. A 128 (8) (2022) 663.

[6] I. Sardar, M.D. Hossain, M.S. Sikder, M.N.I. Khan, M.R. Rahman, Enhancement of coercivity, permeability, and dielectric properties of $Co_{0.2}Zn_{0.3}Ni_{0.5}Eu_xFe_{2-x}O_4$ ferrites for memory and high-frequency devices, J. Rare Earths (2023).

[7] L.Z. Li, X.X. Zhong, R. Wang, X.Q. Tu, L. He, Effects of Al substitution on the properties of NiZnCo ferrite nanopowders, J. Mater. Sci. Mater. Electron. 29 (2018) 7233–7238.

[8] A.B. Mugutkar, S.K. Gore, R.S. Mane, S.M. Patange, S.S. Jadhav, S.F. Shaikh, A. M. Al-Enizi, A. Nafady, B.M. Thamer, M. Ubaidullah, Structural modifications in Co–Zn nanoferrites by Gd substitution triggering to dielectric and gas sensing applications, J. Alloys Compd. 844 (2020), 156178.

[9] N. Jahan, J.I. Khandaker, H. Das, M.N.I. Khan, Structural and magnetic properties analysis of trivalent Al3+ ions substituted Ni-Zn-Co nano-spinel ferrites, Adv. Nat. Sci. Nanosci. Nanotechnol. 12 (4) (2021), 045001.

[10] G.V. Priya, N. Murali, J.M. Sailaja, V. Ragavendra, D. Parajuli, P.L. Narayana, Al3+ and Cr3+ co-substituted NiZnCo nano ferrites: synthesis and structural properties, in: IOP Conference Series: Materials Science and Engineering, Vol. 1233, No. 1, IOP Publishing, 2022, p. 012010.

[11] P. Himakar, K. Jayadev, D. Parajuli, N. Murali, P. Taddesse, S.Y. Mulushoa, T. W. Mammo, B. Kishore Babu, V. Veeraiah, K.J.A.P.A. Samatha, Effect of Cu substitution on the structural, magnetic, and dc electrical resistivity response of $Co_{0.5}Mg_{0.5\text{-}x}Cu_xFe_2O_4$ nanoferrites, Appl. Phys. A 127 (5) (2021) 371.

[12] A. Ramakrishna, N. Murali, T.W. Mammo, K. Samatha, V. Veeraiah, Structural and DC electrical resistivity, magnetic properties of Co0.5M0.5Fe2O4 (M= Ni, Zn, and Mg) ferrite nanoparticles, Physica B: Condensed Matter 534 (2018) 134–140.

[13] A. Ramakrishna, N. Murali, S.J. Margarette, K. Samatha, V. Veeraiah, Comparative study of synthesis, structural and magnetic properties of Cu2+ substituted Co-Ni, Co-Zn and Co-Mg nano ferrites, Physica B: Condensed Matter 530 (2018) 251–257.

[14] M.P. Reddy, G. Balakrishnaiah, W. Madhuri, M.V. Ramana, N.R. Reddy, K. S. Kumar, V.R.K. Murthy, R.R. Reddy, Structural, magnetic and electrical properties of NiCuZn ferrites prepared by microwave sintering method suitable for MLCI applications, J. Phys. Chem. Solid 71 (9) (2010) 1373–1380.

[15] X. Zhou, Y. Zhou, L. Zhou, J. Wei, J. Wu, D. Yao, Effect of Gd and La doping on the structure, optical and magnetic properties of NiZnCo ferrites, Ceram. Int. 45 (5) (2019) 6236–6242.

[16] C. Komali, N. Murali, K. Rajkumar, A. Ramakrishna, S. Yonatan Mulushoa, D. Parajuli, P.N.V.V.L. Pramila Rani, S. Ampolu, K. Chandra Mouli, Y. Ramakrishna, Probing the DC electrical resistivity and magnetic properties of mixed metal oxides Cr3+ substituted Mg–Zn ferrites, Chem. Pap. 77 (1) (2023) 109–117.

[17] K. Chandramouli, V. Raghavendra, P.P. Varma, B. Suryanarayana, T.W. Mammo, D. Parajuli, P. Taddesse, N. Murali, Influence of Cr3+-substituted Co0.7Cu0.3Fe2-xCrxO4 nanoferrite on structural, morphological, dc electrical resistivity and magnetic properties, Appl. Phys. A 127 (2021) 1–14.

[18] H.R. Daruvuri, N. Murali, M. Madhu, A. Ramakrishna, D. Parajuli, M.P. Dasari, Effects of Zn2+ substitution on the structural, morphological, DC electrical resistivity, permeability and magnetic properties of Co0.5Cu0.5-xZnxFe2O4 nanoferrite, Appl. Phys. A 129 (1) (2023) 61.

[19] Z. Zheng, X. Wu, Q. Feng, V.G. Harris, Low loss and tailored high-frequency performances of BaO-doped NiZnCo magneto-dielectric ferrites, J. Am. Ceram. Soc. 103 (2) (2020) 1248–1257.

[20] X. Wu, J. Xu, X. Huo, J. Chen, Q. Zhang, F. Huang, Y. Li, H. Su, L. Li, Nb_2O_5-doped NiZnCo ferrite ceramics with ultra-high magnetic quality factor and low coercivity for high-frequency electronic devices, J. Eur. Ceram. Soc. 41 (10) (2021) 5193–5200.

[21] H.S. Guo, L.Z. Li, X.H. Wu, Z.C. Zhong, Z.X. Tao, F.H. Wang, T. Wang, Enhanced of the resonant frequency of NiZnCo ferrites induced by the substitution of Fe ions with Gd ions, J. Magn. Magn. Mater. 538 (2021), 168249.

[22] Z.C. Zhong, L.Z. Li, X.H. Wu, X.X. Zhong, Z.X. Tao, H.S. Guo, F.H. Wang, T. Wang, Influence of Nd substitution on the structural, magnetic and electrical properties of NiZnCo ferrites, Ceram. Int. 47 (7) (2021) 8781–8786.

[23] S.K. Gore, R.S. Mane, M. Naushad, S.S. Jadhav, M.K. Zate, Z.A. Alothman, B.K. Hui, Influence of Bi 3+-doping on the magnetic and Mössbauer properties of spinel cobalt ferrite, Dalton Trans. 44 (14) (2015) 6384–6390.

[24] R.A. Pawar, S.M. Patange, A.R. Shitre, S.K. Gore, S.S. Jadhav, S.E. Shirsath, Crystal chemistry and single-phase synthesis of Gd 3+ substituted Co–Zn ferrite nanoparticles for enhanced magnetic properties, RSC Adv. 8 (44) (2018) 25258–25267.

[25] X.H. Wu, L.Z. Li, X.X. Zhong, R. Wang, X.Q. Tu, L. He, F.H. Wang, Effects of HfO2 dopant on the structure, magnetic and electrical properties of NiZnCo ferrites, Ceram. Int. 45 (8) (2019) 10776–10781.

[26] H.S. Guo, L.Z. Li, R. Wang, Z. Xiong, Y.L. Yan, Z.C. Zhong, X. Chang, Cd-substituted NiZnCo ferrite with high dielectric constant and low coercivity for high-frequency electronic devices, Ceram. Int. 48 (3) (2022) 3609–3614.

[27] D.L. Navgare, V.B. Kawade, U.B. Tumberphale, S.S. Jadhav, R.S. Mane, S.K. Gore, Superparamagnetic cobalt-substituted copper zinc ferrialuminate: synthesis, morphological, magnetic and dielectric properties investigation, J. Sol-Gel Sci. Technol. 93 (2020) 633–642.

[28] C. Stergiou, Magnetic, dielectric and microwave absorption properties of rare earth doped Ni–Co and Ni–Co–Zn spinel ferrites, J. Magn. Magn. Mater. 426 (2017) 629–635.

[29] X. Shen, Y. Wang, X. Yang, L. Lu, L. Huang, 0.3–3 GHz magneto-dielectric properties of nanostructured NiZnCo ferrite from hydrothermal process, J. Mater. Sci. Mater. Electron. 21 (2010) 630–634.

[30] P. Samoila, L. Sacarescu, A.I. Borhan, D. Timpu, M. Grigoras, N. Lupu, M. Zaltariov, V. Harabagiu, Magnetic properties of nanosized Gd doped Ni–Mn–Cr ferrites prepared using the sol–gel auto-combustion technique, J. Magn. Magn. Mater. 378 (2015) 92–97.

[31] A. Kumar, M.K. Gora, G. Lal, B.L. Choudhary, P.L. Meena, R.S. Dhaka, R.K. Singhal, S. Kumar, S.N. Dolia, Impact of Gd3+ doping on structural, electronic, magnetic, and photocatalytic properties of MnFe2O4 nanoferrites and application in dye-polluted wastewater remediation, Environ. Sci. Pollut. Res. 30 (7) (2023) 18820–18842.

[32] B. Madhavilatha, D. Parajuli, K. Jayadev, C. Komali, N. Murali, V. Veeraiah, K. Samatha, Effect of Cu substitution on magnetic properties of $Co_{0.6}Ni_{0.4}Fe_2O_4$ nanoferrites, Biointerface Res. Appl. Chem. 12 (2021) 1899–1906.

[33] A.B. Mugutkar, S.K. Gore, U.B. Tumberphale, V.V. Jadhav, R.S. Mane, S. M. Patange, S.E. Shirsath, S.S. Jadhav, Role of composition and grain size in controlling the structure sensitive magnetic properties of Sm3+ substituted nanocrystalline Co-Zn ferrites, J. Rare Earths 38 (10) (2020) 1069–1075.

[34] D. Hebbar, K.S. Choudhari, N. Pathak, S.A. Shivashankar, S.D. Kulkarni, Microwave-assisted synthesis of $ZnGa_{2-x-y}Eu_xTb_yO_4$ luminescent nanoparticles showing balanced white-light emission, New J. Chem. 46 (13) (2022) 6103–6113.

[35] S.K. Gore, U.B. Tumberphale, S.S. Jadhav, S.F. Shaikh, A.M. Al-Enizi, A.U.H. S. Rana, R.N. Khule, S.D. Raut, T.S. Gore, R.S. Mane, Grain and grain boundaries influenced magnetic and dielectric properties of lanthanum-doped copper cadmium ferrites, J. Mater. Sci. Mater. Electron. 33 (10) (2022) 7636–7647.

[36] D.L. Navgare, V.B. Kawade, S.F. Shaikh, S.S. Jadhav, U.B. Tumberphale, R. N. Khule, R.S. Mane, S.K. Gore, Structure-sensitive magnetic properties of nanocrystalline Co2+-substituted Ni–Zn ferrite aluminates, Ceram. Int. 47 (18) (2021) 26492–26500.

[37] G.V. Priya, S.R. Kumar, B. Aruna, M.K. Raju, D. Parajuli, N. Murali, P.V. L. Narayana, Effect of Al3+ substitution on structural and magnetic properties of NiZnCo nano ferrites, Bionterface Res. Appl. Chem 12 (2022) 6094–6099.

[38] K.L.V. Nagasree, B. Suryanarayana, V. Raghavendra, S. Uppugalla, T.W. Mammo, D. Kavyasri, N. Murali, M.K. Raju, D. Parajuli, K. Samatha, Influence of Mg2+ and Ce3+ substituted on synthesis, structural, morphological, electrical, and magnetic properties of Cobalt nano ferrites, Inorg. Chem. Commun. (2023), 110405.

[39] D. Parajuli, N. Murali, A.V. Rao, A. Ramakrishna, K. Samatha, Structural, DC electrical resistivity and magnetic investigation of Mg, Ni, and Zn substituted Co-Cu nano spinel ferrites, S. Afr. J. Chem. Eng. 42 (2022) 106–114.

[40] K. Chandramouli, P.A. Rao, B. Suryanarayana, V. Raghavendra, S.J. Mercy, D. Parajuli, P. Taddesse, S.Y. Mulushoa, T.W. Mammo, N. Murali, Effect of Cu substitution on magnetic and DC electrical resistivity properties of Ni–Zn nanoferrites, J. Mater. Sci. Mater. Electron. 32 (12) (2021) 15754–15762.

[41] M. Madhu, A.V. Rao, D. Parajuli, S.Y. Mulushoa, N. Murali, Cr3+ substitution influence on structural, magnetic and electrical properties of the Ni0.3Zn0.5Co0.2Fe2-xCrxO4 (0.00≤ x≤ 0.20) nanosized spinel ferrites, Inorg. Chem. Commun. 143 (2022), 109818.

[42] R.V. Bharathi, M.K. Raju, S. Uppugalla, V. Raghavendra, D. Parajuli, B. Suryanarayana, S.Y. Mulushoa, N. Murali, K. Samatha, Cu2+ substituted Mg-Co ferrite has improved DC electrical resistivity and magnetic properties, Inorg. Chem. Commun. 149 (2023), 110452.

Inorganic Chemistry Communications 165 (2024) 112480

Contents lists available at ScienceDirect

Inorganic Chemistry Communications

journal homepage: www.elsevier.com/locate/inoche

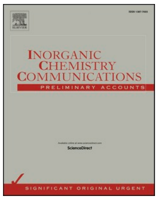

Short communication

Effect of rare earth (Sm^{3+}) substitution in mixed Ni-Zn-Co ferrites: Structural, magnetic, and DC electrical resistivity studies

Tejeswararao Reddy [a], Sivasankar Reddy Akepati [a,*], V. Nagalakshmi [b], D. Jagadeeswara Rao [c,*], Ramakrishna Madaka [d]

[a] Department of Physics, Vikram Simhapuri University College, Kavali, Andhra Pradesh, India
[b] Department of Chemistry, Ch. S. D. St. Theresa's College for Women (A), Eluru, A.P., India
[c] Department of Physics, S.V. Govt. Degree College, Parvathipuram, Andhra Pradesh, India
[d] Department of Physics, School of Sciences, Woxsen University, Hyderabad, Telangana, India

ARTICLE INFO

Keywords:
NiZnCo ferrite
Spinel structure
FTIR spectra
Magnetic measurements
Resistivity

ABSTRACT

NiZnCo ferrite has good magnetic properties and is one of the core materials used in magnetic devices. The solid-state reaction approach is utilized to synthesize $Ni_{0.4}Zn_{0.35}Co_{0.25}Fe_{2\text{-}x}Sm_xO_4$ (x = 0.0, 0.02, 0.04, 0.06, 0.08, and 0.1) ferrites for investigation of structural, morphological, functional, magnetic and electrical resistivity properties using various characterization techniques. The techniques used for characterization were XRD, SEM, FTIR, VSM, and DC electrical resistivity. XRD spectra were used to determine phase confirmation, cubic crystallite size, and their variation with dopant content. No additional phase or impurity was found. The SEM pictures revealed a homogeneous spherical particle formation with minimal porosity. With absorption bands under 1000 cm^{-1}, FTIR spectra indicate the formation of a spinel structure. Tetrahedral (580 to 599 cm^{-1}) and octahedral (388 to 399 cm^{-1}) bond changes can be seen in infrared spectra. The magnetic hysteresis curves revealed soft ferromagnetic behavior, with coercivity (Oe) (532.13 to 312.10 Oe) rising and saturation magnetization (Ms) (83.51 to 60.75 emu/g) falling as doping concentration increased. The DC electrical resistivity of synthesized nanoparticles with various compositions was measured against higher temperatures to confirm their semiconductor nature. The findings demonstrated the typical decreasing trend with rising temperature.

1. Introduction

Superconducting, dielectric, and hybrid ferrite materials are crucial for electronic devices. Soft spinel ferrites have garnered significant interest due to their distinctive properties, including low loss and coercivity with high resistivity [1]. Ferrites from the NiZn series are commonly utilized in various applications such as switches, multilayer chip inductors, antenna coils, ceramic capacitors, flux guidance, and multilayer chip inductors [2,3]. Adding the magnetic ion Co^{2+} to NiZnCo ferrites has been observed to reduce losses, increase saturation magnetization, and enhance resistivity. This, coupled with their ability to absorb visible light, positions NiZnCo ferrites favourably as semiconductor photocatalysts compared to spinel ferrites [4]. Their versatile applications, including medication administration, magnetic storage devices, sensors, and permanent magnets, contribute to their growing popularity [5].

Rare earth ions, also known as doping replacement ions, are utilized to enhance the magnetic characteristics of materials. The electromagnetic properties of a material can be improved by incorporating rare earth ions with distinctive electromagnetic properties [6]. The intrinsic magnetic properties of spinel can be influenced by the saturation magnetization strength and resistivity of rare earth ions and their 3d electrons [7]. For instance, Y^{3+} decreases magnetic loss and exhibits a higher frequency shift, while Pr^{3+} increases the dielectric constant, and Sm^{3+} demonstrates the least dielectric constant. Gd^{3+} also reduces grain size while increasing saturation magnetization strength and coercivity [8–11]. Various synthesis methods can create NiCoZn ferrite-based materials [1]. The solid-state reaction method is preferred for synthesizing NiCoZn materials because it yields pure, homogeneous, and uniform materials [12]. For example, the ceramic method was utilized by the group led by D. Parajuli et al. to synthesize transition-metal-doped $Li_{0.5}Fe_{2.5}O_4$ ferrites, and they reported enhanced magnetic parameters for the synthesized materials [13]. The S.S. Kadam et al. group has also investigated rare earth element doping using the sol–gel route. They

---

* Corresponding authors.
E-mail addresses: akepati77@gmail.com (S. Reddy Akepati), dasarijagadeesh@gmail.com (D. Jagadeeswara Rao).

https://doi.org/10.1016/j.inoche.2024.112480
Received 22 December 2023; Received in revised form 11 April 2024; Accepted 27 April 2024

examined the structural, magnetic, and dielectric properties of Ce^{3+} substitution in the Co-Cr-Fe-O nano ferrite host material [14]. Similarly, the group led by B. Suryanarayana et al. conducted a study on rare earth cation doping. Besides investigating structural and morphological characteristics, they explored DC electrical resistivity and magnetic properties, suggesting potential high-frequency applications for the synthesized materials [15].

Furthermore, prior research showed that NiZnCo ferrite samples sintered using ceramic have better magnetic characteristics than standard sintering methods. Overall, nano ferrite materials' characteristics significantly depend on chemical composition, synthesis method, and other external parameters [16]. In this study, $Ni_{0.4}Zn_{0.35}Co_{0.25}$-$Fe_{2-x}Sm_xO_4$ for x = 0.0, 0.02, 0.04,0.06, 0.08, and 0.1 ferrite materials were ceramic sintered at 1050^0C. Then there's the effect of Sm^{3+} doping on the microstructure. Previous research has indicated that NiZnCo ferrite samples sintered using the ceramic method exhibit superior magnetic characteristics compared to standard sintering methods. The characteristics of nanoferrite materials are significantly influenced by chemical composition, synthesis method, and other external parameters [16].

In this study, $Ni_{0.4}Zn_{0.35}Co_{0.25}Fe_{2-x}Sm_xO_4$ ferrite materials with x = 0.0, 0.02, 0.04, 0.06, 0.08, and 0.1 were ceramic sintered at 1050 °C. Subsequently, the effect of Sm^{3+} doping on the structural, microstructural, DC electrical, and magnetic properties was investigated. To the best of researchers' understanding, less work is available at the mentioned level of doping these materials.

2. Experimental studies

The Merck limited analytical grade 98 % pure oxides of Nickel, Zinc, Cobalt, Samarium, and Iron are used as starting materials to make $Ni_{0.4}Zn_{0.35}Co_{0.25}Fe_{2-x}Sm_xO_4$ for x = 0.0, 0.02, 0.04,0.06, 0.08 and 0.1 solid state approach. When ground for 8 h, adding acetone effects in a homogeneous mixture that gives the as-prepared sample. The product was calcined at 900 °C for 3 h, grounded for 3 h, sintered at 1050 °C for 4 h, and grounded for 3 h.

The morphology of the synthesized powders was examined using SEM: JEOL, JSM-6490LV; FTIR spectrometer (Bruker VERTEX70) in the range 4000 cm^{-1} to 400 cm^{-1} gives FTIR spectra; an XRD diffractometer (XRD: DX-2700, Haoyuan) gives their crystal structure. The resistivity of each sample is measured using a two-probe DC resistivity device (TPX-200C). The hydraulic press produced a pellet with 12 mm x 2 mm dimension using a 5 ton/cm2 pressure for all electrical measurements. With silver conducting paste obtained from Sigma Aldrich, two electrodes were linked on either side of the pellet. A thin layer of silver paste was also applied on both sides of the pellet.

3. Results and discussion

3.1. XRD analysis

Fig. 1 shows the XRD patterns for ferrites with $Ni_{0.4}Zn_{0.35}Co_{0.25}$-$Fe_{2-x}Sm_xO_4$ for x = 0.0, 0.02, 0.04,0.06, 0.08, and 0.1. The primary spinel diffraction peaks (2) are produced by the (220), (311), (222), (400), (422), (511), and (440) planes of a single-phase cubic spinel structure with Fd3m group [17]. The figure's marked diffraction peaks are matched with PDF#97–018-4940, which agrees with the crystallographic indices [18]. The fact that the radii of Sm^{3+} (0.964 Å) are more extensive or greater than Fe^{3+} (0.64 Å) ions [19]. In contrast, the lattice parameter decreases following Sm^{3+} doping levels. Ionic radius has brought more of an impact and microstrain. Additionally, the lattice constant drops when the rare earth's atomic number increases and ionic radii decrease. This demonstrates how rare earth metals can replace Fe^{3+}. Table 1 shows measured parameters. Due to Sm^{3+} filling the crystal lattice's gaps, the grid points in the crystal expand [20]. The XRD (311) peak in Fig. 2 is magnified, showing how the peaks broaden as the Sm^{3+} concentration rises. The presence of trivalent ions in the spinel structure indicates the examined samples' ultra-fine nature and small crystallite size.

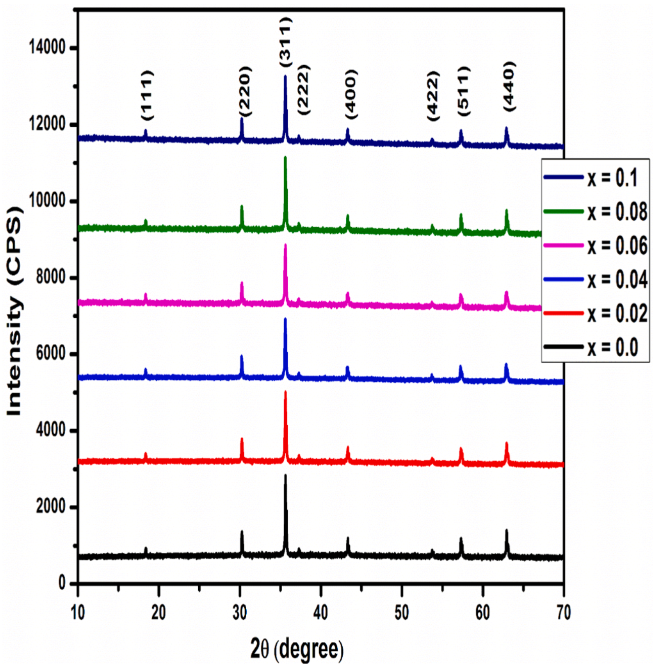

Fig. 1. XRD patterns of $Ni_{0.4}Zn_{0.35}Co_{0.25}Fe_{2-x}Sm_xO_4$.

The lattice constant falls as the doping level increases. The following formula is used to determine the cell parameter [21]:

$$\mathbf{a} = \mathbf{d_{hkl}}\sqrt{\mathbf{h}^2 + \mathbf{k}^2 + \mathbf{l}^2}$$

Therefore, d_{hkl} is the increased interplane separation for the specified hkl planes, according to Bragg's law.

The variation of the average crystallite size and lattice parameter with increasing Sm^{3+} doping levels is shown in Fig. 3. The altered lattice constant reflects the crystal's interior structure and stress condition. The proportionate size of the grain growth rate and the quantity of crystal nuclei determine the average crystallite size given by the Scherrer equation [22].

$$\boldsymbol{D}_{311} = \frac{0.9\lambda}{\boldsymbol{\beta cos\theta}}$$

when $\boldsymbol{\theta}$ – the diffraction angle, $\boldsymbol{\beta}$ – the complete width at half maximum of the (311) peak, $\boldsymbol{\lambda}$ – the X-ray wavelength (1.5406) are all considered.

The sample's X-ray density, or "x", can be determined using the formula below [18].

$$\rho_x = \frac{ZM}{N_A a^3}$$

The unit cell of the spinel crystal lattice has the sublattice number "Z = 8." 'M' stands for the molecular weight of the sample at various doping concentrations. On the other hand, the Avogadro constant, which has a value of 6.02 x 10^{23}, is 'NA' [20].

$$\rho_b = \frac{m}{\pi^2 RT}$$

The sample's bulk density ("ρb") can be computed using the formula above. The symbols 'm' denote sample mass, 'R' sample radius, and 't' sample thickness.

Accordingly, the sample's porosity ('P') can be computed using the method below [23].

Table 1
Lattice parameters of $Ni_{0.4}Zn_{0.35}Co_{0.25}Fe_{2-x}Sm_xO_4$ ferrite system.

Concentration	Lattice constant (Å)	Crystallite size (nm)	Molecular weightM (g/mol)	X-ray density ρ_x (g cm^3)	Bulk Density ρ_b(g/cm^3)	Porosity P (%)	Grain sizes (μm)
0.0	8.382	40.56	236.78	5.343	5.071	5.1	1.90
0.02	8.381	37.65	238.68	5.388	4.969	7.8	1.85
0.04	8.379	34.98	240.57	5.434	4.936	9.2	1.79
0.06	8.377	29.85	242.46	5.481	4.921	10.2	1.77
0.08	8.375	27.54	244.35	5.523	4.784	13.4	1.75
0.1	8.373	25.25	246.24	5.575	4.645	16.7	1.70

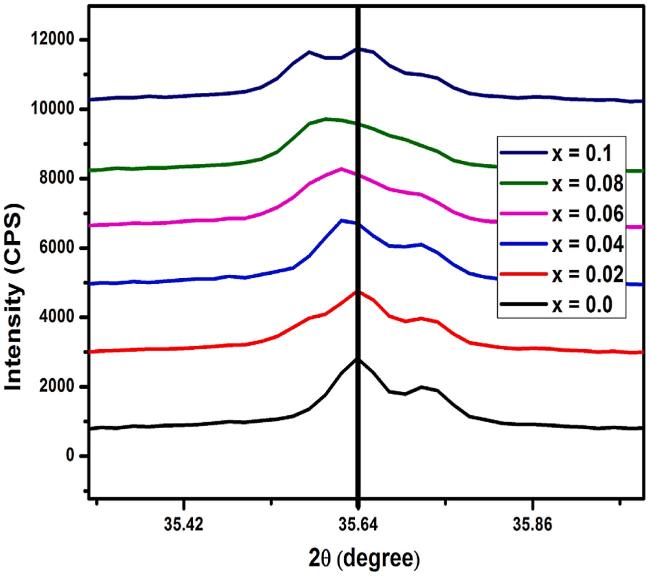

Fig. 2. Shift in peak positionEnlarged view of peak shift position of the (3 1 1) Bragg peak of $Ni_{0.4}Zn_{0.35}Co_{0.25}Fe_{2-x}Sm_xO_4$.

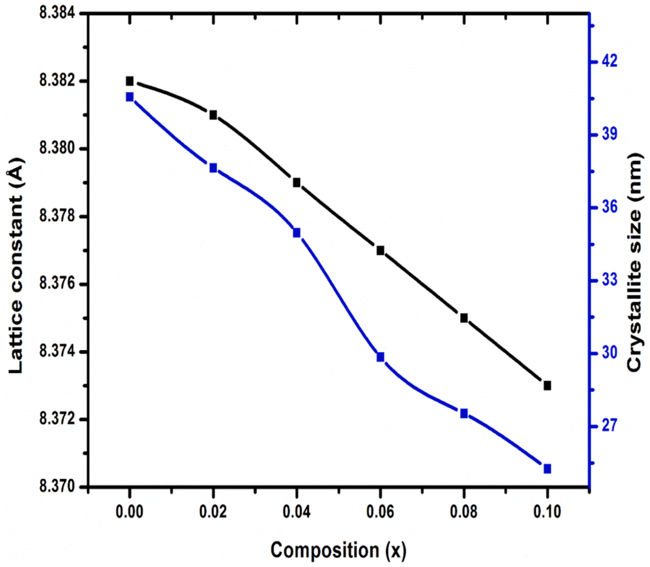

Fig. 3. Lattice constant and Crystallite size curves of $Ni_{0.4}Zn_{0.35}Co_{0.25}Fe_{2-x}Sm_xO_4$.

$$P = \left(1 - \frac{\rho_b}{\rho_x}\right) \times 100$$

The bulk and X-ray densities mainly determine the properties of polycrystalline ferrites. The effects of Sm^{3+} ions on the bulk densities, porosities, and X-ray densities are displayed in Table 1. During the synthesis process, pores occur inside the crystal structures of the samples. As a result, the composition shows lower bulk densities than anticipated (X-ray) densities (Table 1). As the dopant concentration rises, the Sm^{3+} contents have led to a modest increase in the X-ray densities. Samples' porosities, P (%), can be explained by their intragranular porosity (Pintra) and intergranular porosity (Pinter). Intragranular porosity refers to pores or voids within the ferrite material's grains or crystal structure and is typically smaller in size.

In contrast, the intergranular porosities are pores or voids at the boundaries between adjacent grains in the ferrite material. During sintering, the heat energy acts as a force, forcing the grain boundaries to form across the pores. The decreased pore volume causes the material to grow denser. The effects of the compositions on intragranular porosities were insignificant since the sintering temperature of the produced ferrites was constant throughout the investigations. Because of the uneven particles, intergranular porosities develop inside the ferrites during sintering. After that, there is an inverse relationship between the compositions' bulk densities and porosities. In Table 1, the intergranular porosities are mentioned. Furthermore, the pores permit the diffusion of cations within and surrounding the pores and the passage of gaseous oxygen. Because there are more cation vacancies and less oxygen, the porosities of the ferrites under study increase with Sm^{3+} concentrations.

3.2. SEM analysis

The SEM pictures of the ferrite samples $Ni_{0.4}Zn_{0.35}Co_{0.25}Fe_{2-x}Sm_xO_4$ are displayed in Fig. 4. The sample has huge grains, but it also contains some smaller grains. Because of this, the grain size distribution is irregular, and the pores are noticeable when x = 0. There are fewer holes and a higher sample density due to the more uniform grain size distribution [19]. However, the microscopic view clearly shows a lot of tiny granules. Due to the dual organization of tiny and large grains at this stage, many pores occur, and the density is reduced [24]. The composition takes place from 1.7 to 1.9 μm, and the calculated average grain size from SEM images shows a declining tendency. Empirical research reveals that ferrite samples synthesized with Sm^{3+} added exhibit smaller grains than pure NiZnCo ferrite. Smaller grains are produced, and less energy is needed for crystallization because the Fe-O bond forms more quickly than the Sm-O link. The values of the grain sizes were calculated by employing the ImageJ application software.

3.3. FTIR analysis

$Ni_{0.4}Zn_{0.35}Co_{0.25}Fe_{2-x}Sm_xO_4$ synthesized samples' FTIR spectra were seen at room temperature, supporting the formation of the spinel structure. Two distinguishing absorption bands were consistently seen in the 400 cm^{-1} to 4000 cm^{-1} frequency range, as shown in Fig. 5. These bands are consistent with those previously described for the same ferrite

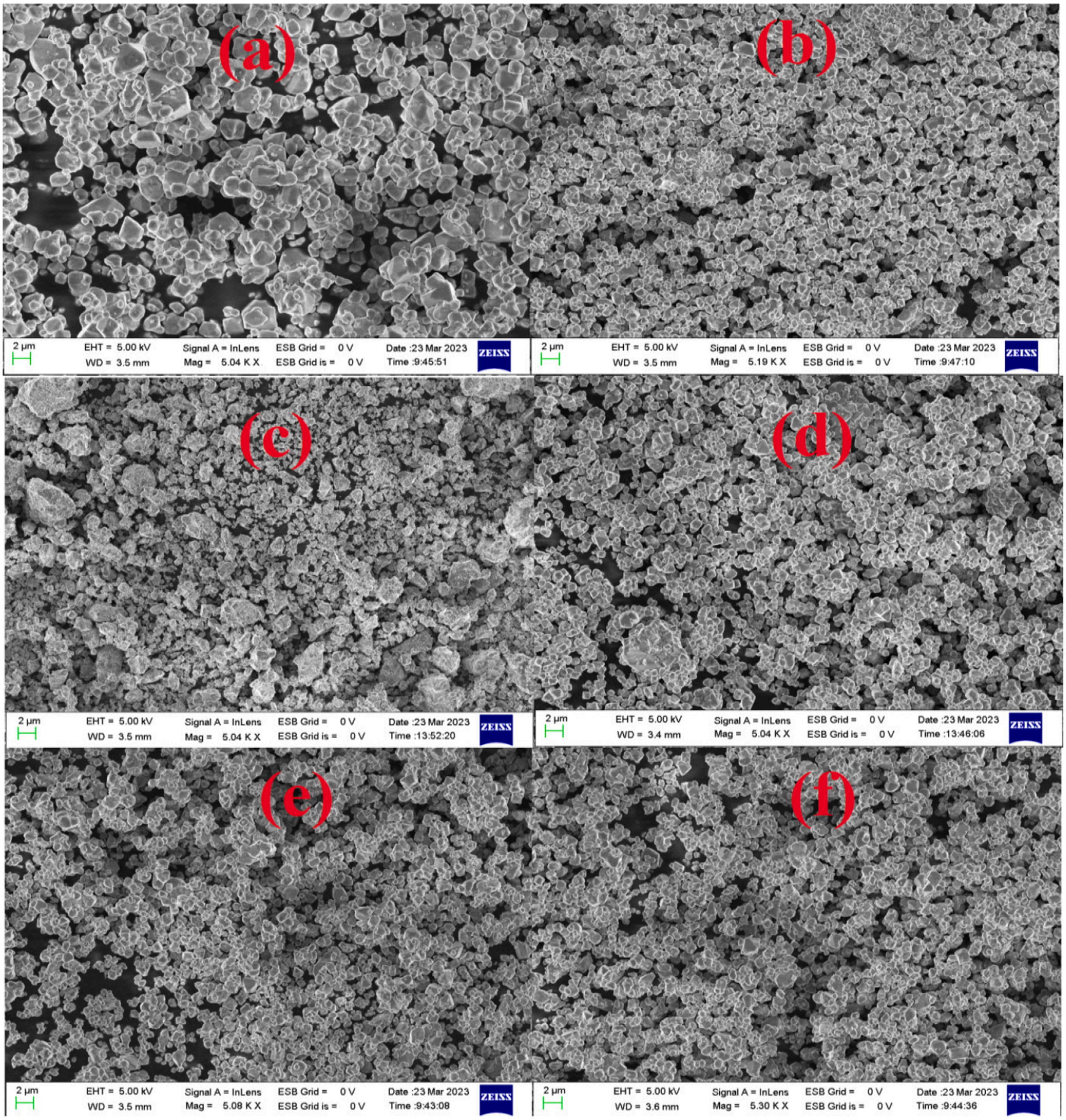

Fig. 4. SEM patterns of representative samples for $Ni_{0.4}Zn_{0.35}Co_{0.25}Fe_{2-x}Sm_xO_4$ (a) for x = 0, (b) for x = 0.02, (c) for x = 0.04, (d) for x = 0.06, (e) for x = 0.08, and (f) for x = 0.1).

family [25]. Since the tetrahedral (A) and octahedral (B) positions of the metal ions in ferrites are different from one another, stretching these geometrical sites results in a band of roughly 600 cm^{-1} for the intrinsic tetrahedral metal complex and a band of about 400 cm^{-1} for the intrinsic octahedral metal complex. These lattice arrangements show that spinel structural growth has occurred [26]. According to metal–oxygen ion stretching vibrations at the A-site, the samples' highest absorption peak formation occurred at 580 to 599 cm^{-1}. In contrast, the samples' lowest absorption peak formation occurred at 388 to 399 cm^{-1}, according to the metal–oxygen ion stretching vibrations at the B-site values tabulated in Table 2. The less important absorption peaks at higher frequency ranges of 1200–1750 cm^{-1}, which correspond to the O–H bending bond, could be mentioned [27].

3.4. *VSM analysis*

The M−H hysteresis loop of $Ni_{0.4}Zn_{0.35}Co_{0.25}Fe_{2\text{-}x}Sm_xO_4$, where x = 0.0, 0.02, 0.04, 0.06, 0.08, and 0.1, ferrites, was measured at ambient temperature using a vibrating sample magnetometer (VSM). This analysis aimed to investigate the magnetic response of the samples designed to withstand an external magnetic field. Fig. 6 illustrates the resulting M−H curves, while Table 3 details magnetic properties derived from these curves. These properties include saturation magnetization (Ms), remanent magnetization (Mr), coercivity (Hc), and remanence ratio (R).

The magnetization value decreases as Sm^{3+} ions replace Fe^{3+} ions, owing to the lower magnetic moment of Sm^{3+} ions. In the lattice of the prepared samples, RE^{3+} ions (Sm^{3+}) preferentially occupy the B site, replacing the Fe^{3+} ion at the octahedral site [28].

Furthermore, crucial properties such as crystallite size have been identified as influencing the magnetic field's region and diminishing

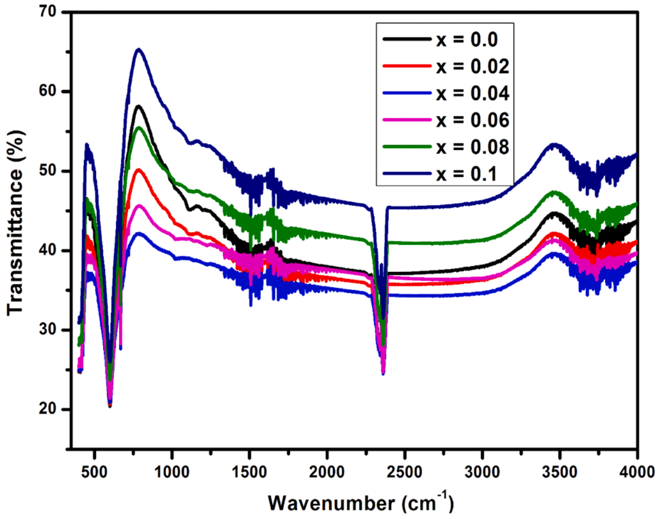

Fig. 5. FTIR spectra of synthesized $Ni_{0.4}Zn_{0.35}Co_{0.25}Fe_{2-x}Sm_xO_4$.

Table 2
Octahedral ($\upsilon2$) and tetrahedral ($\upsilon1$) absorption bands of $Ni_{0.4}Zn_{0.35}Co_{0.25}Fe_{2-x}Sm_xO_4$.

Composition (x)	Octahedral absorption band ($\upsilon2$)	tetrahedral absorption band ($\upsilon1$)
0.0	580	388
0.02	583	391
0.04	589	395
0.06	594	396
0.08	597	398
0.1	599	399

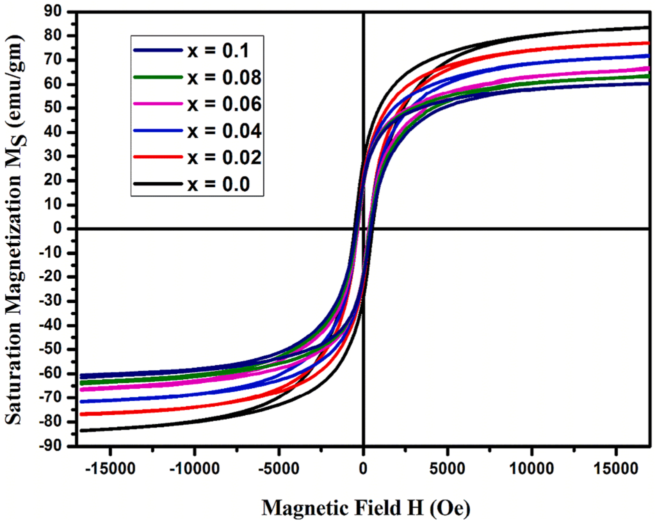

Fig. 6. Hysteresis loops of $Ni_{0.4}Zn_{0.35}Co_{0.25}Fe_{2-x}Sm_xO_4$.

magnetization, as indicated by previous studies [29,30]. This phenomenon arises as the size of the crystallites or grains increases, resulting in fewer obstacles and a more pronounced magnetic nature. In addition to crystallite size, three other factors impacting magnetism are 3d-4f coupling and spin–orbit coupling [31]. This may occur during a phenomenon referred to as superexchange interaction due to the site confinement of interacting cations [32]. The effect of spin–orbit coupling plays a significant role in controlling the magnetization of RE^{3+} ions [33]. In general, the influence of Sm^{3+} in these current materials is to yield tuned values of the magnetic parameters.

As the concentration of Sm^{3+} ions increases, the Ms value decreases. When RE^{3+} ions (expressly, the Sm^{3+} ions) are incorporated into the synthesized samples, it appears that the magnetic Fe^{3+} ions in the spinel lattice's octahedral location are replaced with non-magnetic atoms [34]. Consequently, the reduction in room temperature magnetization becomes evident with the escalating RE^{3+} content. The gradual decrease in Ms with an increasing Sm^{3+} concentration may also be attributed to the smaller particle size of Sm^{3+}-substituted NiZnCo ferrite. The prepared samples' coercivity (Hc) is influenced by their size, shape, microstrain, and magneto-crystalline anisotropy [35]. For x = 0.0, the maximum coercivity (Hc) reached was 532.13 Oe, while the minimum value obtained was 312.10 Oe. In this case, the lower degree of magnetic anisotropy resulted in lower coercivity (Hc) and higher saturation magnetization (Ms).

In addition, the amount of the remanent magnetization (Mr), initially 29.89 emu/g, decreased as dopants were added. The coercivity and saturation magnetization of the artificial ferrite are shown in Fig. 6. A multi-domain structure formed in the synthesized nanomaterials due to the calculated aspect ratio (Mr/Ms) being less than 0.5 [36]. The magnetic moment value (nB) for the synthesized nano ferrites was determined to range between 3.54 and 2.68 μB, utilizing the equation presented below [37], and Table 3 summarizes the calculated values.

$$\eta_B = \frac{M_s \times M.W}{5585}$$

where M.W. denotes the molecular weight of the synthetic sample, and Ms stands for saturation magnetization. The manufactured samples' magnetic moment (nB) and Ms have a strong correlation; as Ms decreases, so does the value of η_B.

3.5. DC resistivity analysis

Several factors, including the synthesis process, sintering, grain size, porosity, density, and chemical composition, frequently influence the electrical resistivity of ferrites. Electrical properties such as conductivity or resistance are typically influenced by electron hopping between ions of the same element with various valence states [38–42]. In other words, variations in DC resistivity are attributed to the cationic dispersion in the spinel structure. Fig. 7 illustrates the measurement of DC resistivity using the two-probe method for $Ni_{0.4}Zn_{0.35}Co_{0.25}Fe_{2-x}Sm_xO_4$, where x = 0.0, 0.02, 0.04, 0.06, 0.08, and 0.1 ferrite compositions synthesized, as a function of temperature. With the substitution of Sm^{3+}, DC resistivity demonstrates a linear decrease with increasing temperature, resulting in an overall increase in resistivity [43–45]. The decrease in resistivity with rising temperature, as depicted in the figure, indicates the semiconducting nature of the samples, which is evident from the graph [46–48].

Moreover, it has been observed that samples with higher concentrations of Sm exhibit greater resistivity, indicating a decrease in the leakage behavior of the samples. B-B electron hopping influences conduction significantly, as A-A electron hopping is prohibited for Fe^{3+} ions confined to octahedral sites. B-B electron hopping occurs more frequently due to B sites' closer proximity than A-B sites [49–52]. As previously discussed, Sm^{3+} ions prefer the octahedral B site. Consequently, as the concentration of Sm^{3+} increases, the content of M^{2+} ions (Ni, Zn, Co) on the octahedral site decreases, leading to the migration of Fe^{3+} ions from the B site to the A site. This shift increases resistivity because fewer Fe^{2+} and Fe^{3+} ions are available at the B site, where conduction via electron hopping predominantly occurs [53]. Additionally, the maximum electron transfer, facilitated by high lattice vibrations at elevated temperatures, encourages ions to approach each other for more effortless electron transfer, thereby promoting conduction at high temperatures. This phenomenon can explain the general decrease in resistivity with increasing temperature [54–56].

To calculate the activation energies of the charge carriers in the

Table 3
Magnetic Saturation, remnant magnetization, coercivity, aspect ratio, and magnetic moment values obtained from M−H curves for $Ni_{0.4}Zn_{0.35}Co_{0.25}Fe_{2-x}Sm_xO_4$.

Composition (x)	Saturation Magnetization (emu/g)	Remnant magnetization (emu/g)	Coercivity (Oe)	M_r/M_s	Magnetic moment (μ_B)
0.0	83.51	29.89	532.13	0.36	3.54
0.02	76.63	28.95	498.57	0.38	3.27
0.04	71.54	27.65	427.49	0.39	3.08
0.06	66.15	26.54	396.32	0.40	2.87
0.08	63.29	23.58	343.68	0.37	2.77
0.1	60.75	21.65	312.10	0.36	2.68

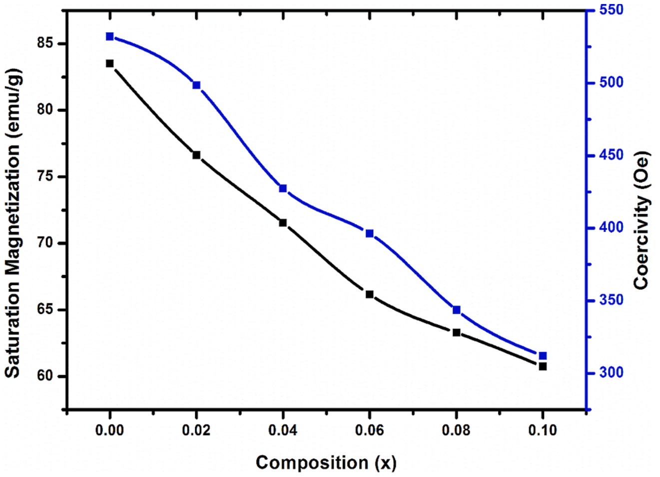

Fig. 7. Magnetic Saturation and Coercivity values variation trends of $Ni_{0.4}Zn_{0.35}Co_{0.25}Fe_{2-x}Sm_xO_4$.

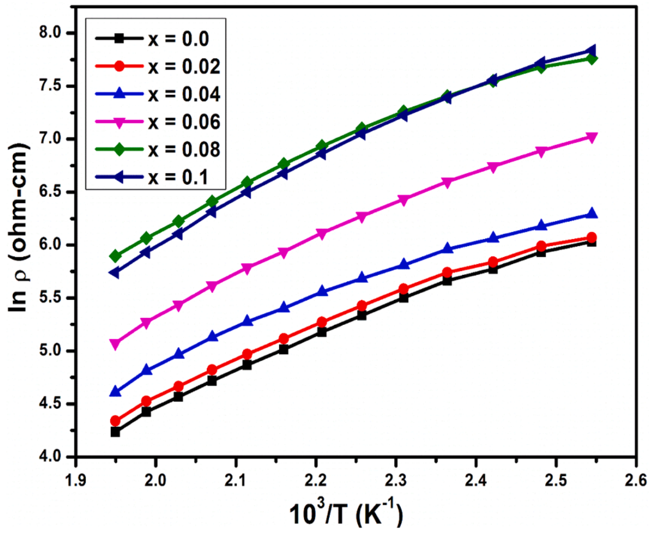

Fig. 8. DC resistivity as a function of temperature.

hopping mechanism described below from the normal semiconducting nature of the Arrhenius formula [57],

$$\rho = \rho_o e^{-\left(\frac{\Delta E}{KT}\right)}$$

where ΔE is the activation energy, and K is the Boltzmann constant. The calculated activation energies of the ferrite nanoparticles are shown in Fig. 8. All samples under examination have activation energies of 0.35, 0.39, 0.42, 0.46, 0.49, and 0.53 eV for synthetic samples, in that order. These low values of activation energy point to the electronic part of the conductivity of the materials. Electrons bounce between the valence states of the same elements dispersed over various sites, per the hopping mechanism outlined by Verwey and de Boer. The estimated activation energy and published data [58] agree.

4. Conclusion

Spinel-structured $Ni_{0.4}Zn_{0.35}Co_{0.25}Fe_{2\text{-}x}Sm_xO_4$, where $x = 0.0$, 0.02, 0.04, 0.06, 0.08, and 0.1 ferrite materials, were successfully synthesized using the solid-state reaction technique and sintered at 1050 °C for 4 h. XRD results demonstrate the formation of an inverted spinel single phase with no impurity phases. As the concentration of the dopant, which ranges from 0.0 to 0.1, increases, the crystallite size (D) is found to increase accordingly. Surface morphology analysis reveals agglomerated spherical-shaped grains. FTIR spectra validate the presence of tetrahedral and octahedral sites in the spinel structure. The saturation magnetization of the ferrite samples demonstrates a propensity to decrease in magnetic characteristics, while the coercivity exhibits a trend to increase.

Additionally, the theory of exchange interactions and Neel's sublattice model have been employed to explain the magnetic moment of the prepared samples, which shows a similar decreasing pattern to saturation magnetization from 3.54 to 2.68 μB. The semiconducting nature of the synthesized compounds is confirmed by the DC resistivity. These versatile spinel systems find potential applications in high-frequency electric circuits, transformers, storage media, and microwave absorption devices, supported by the observed parameters, which also aid in understanding the function of alternative materials.

CRediT authorship contribution statement

Tejeswararao Reddy: Conceptualization, Data curation, Investigation, Formal analysis, Methodology, Writing – original draft. **Sivasankar Reddy Akepati:** Supervision, Formal analysis, Writing – review & editing. **V. Nagalakshmi:** Formal analysis, Writing – review & editing. **D. Jagadeeswara Rao:** Supervision, Formal analysis, Writing – review & editing. **Ramakrishna Madaka:** Formal analysis, Writing – review & editing.

Declaration of competing interest

The authors declare that they have no known competing financial interests or personal relationships that could have appeared to influence the work reported in this paper.

Data availability

The data that has been used is confidential.

References

[1] H.S. Guo, L.Z. Li, X.H. Wu, Z.C. Zhong, Z.X. Tao, F.H. Wang, T. Wang, J. Magn. Magn. Mater. 538 (2021) 168249.
[2] N. Jahan, J.I. Khandaker, H. Das, M.N.I. Khan, Adv. Nat. Sci. Nanosci. Nanotechnol. 12 (4) (2021) 045001.

[3] K. Sakthipandi, B.G. Babu, G. Rajkumar, A. Hossian, M.S. Raghavan, M.R. Kumar, Physica B: Condensed Matter 645 (2022) 414280.
[4] S.R. Kumar, G.V. Priya, B. Aruna, M.K. Raju, D. Parajuli, N. Murali, R. Verma, K. M. Batoo, R. Kumar, P.L. Narayana, Inorg. Chem. Commun. 136 (2022) 109132.
[5] S. Mohammadi, H. Shokrollahi, M.H. Basiri, J. Magn. Magn. Mater. 375 (2015) 38–42.
[6] I.H. Gul, E. Pervaiz, Mater. Res. Bull. 47 (6) (2012) 1353–1361.
[7] S.B. Cho, D.H. Kang, J.H. Oh, J. Mater. Sci. 31 (1996) 4719–4722.
[8] X. Zhou, Y. Zhou, L. Zhou, J. Wei, J. Wu, D. Yao, Ceram. Int. 45 (5) (2019) 6236–6242.
[9] Z. Peng, X. Fu, H. Ge, Z. Fu, C. Wang, L. Qi, H. Miao, J. Magn. Magn. Mater. 323 (20) (2011) 2513–2518.
[10] M.F. Al-Hilli, S. Li, K.S. Kassim, J. Magn. Magn. Mater. 324 (5) (2012) 873–879.
[11] S.E. Jacobo, P.G. Bercoff, Ceram. Int. 42 (6) (2016) 7664–7668.
[12] G.V. Priya, S.R. Kumar, B. Aruna, M.K. Raju, D. Parajuli, N. Murali, P.V. L. Narayana, Bionterface Res. Appl. Chem 12 (2022) 6094–6099.
[13] D. Parajuli, N. Murali, V. Raghavendra, B. Suryanarayana, K.M. Batoo, K. Samatha, Appl. Phys. A 129 (7) (2023) 502.
[14] S.S. Kadam, V.D. More, P.K. Gaikwad, K.M. Batoo, S. Hussain, R.H. Kadam, S. E. Shirsath, A.B. Kadam, Appl. Phys. A 129 (10) (2023) 730.
[15] M. Madhu, A.V. Rao, N. Murali, D. Parajuli, T.W. Mammo, J. Mater. Sci. Mater. Electron. 34 (32) (2023) 2158.
[16] V. Jagadeesha Angadi, K.M. Batoo, S. Hussain, S.O. Manjunatha, S. Wang, S. P. Kubrin, J. Mater. Sci. Mater. Electron. 34 (4) (2023) 301.
[17] G.V. Priya, N. Murali, M.K. Raju, B. Krishan, D. Parajuli, P. Choppara, B.C. Sekhar, R. Verma, K.M. Batoo, P.L. Narayana, Appl. Phys. A 128 (8) (2022) 663.
[18] D. Parajuli, N. Murali, A.V. Rao, A. Ramakrishna, K. Samatha, S. Afr. J. Chem. Eng. 42 (2022) 106–114.
[19] S. Yonatan Mulushoa, N. Murali, M. Tulu Wegayehu, V. Veeraiah, K. Samatha, Mater 13 (2018) 26460–26468.
[20] N. Channa, M. Khalid, A.D. Chandio, G. Mustafa, M.S. Akhtar, J.K. Khan, J. Ahmad, K.A. Kalhoro, J. Mater. Sci. Mater. Electron. 31 (2020) 1661–1671.
[21] S. Yonatan Mulushoa, Ch. VijayaKumari, V. Raghavendra, K.E. Babu, B.S. N. Murthy, K. Suribabu, Y. Ramakrishna, N. Murali, Phys. B. Condens. Matter. 572 (2019) 139–147.
[22] P. Himakar, K. Jayadev, D. Parajuli, N. Murali, P. Taddesse, S.Y. Mulushoa, T. W. Mammo, B. Kishore Babu, V. Veeraiah, K. Samatha, Appl. Phys. A 127 (5) (2021) 371.
[23] Y. Luo, Y. Li, S. Li, M. Qu, Q. Wen, F. Li, J. Magn. Magn. Mater. 570 (2023) 170533.
[24] K.M. Batoo, M. Hadi, A. Chauhan, R. Verma, M. Singh, O.M. Aldossary, G. K. Bhargava, Appl. Phys. A 128 (4) (2022) 283.
[25] M.A. Gabal, J. Phys. Chem. Solid 64 (8) (2003) 1375–1385.
[26] Y. Slimani, R. Sivakumar, S.S. Meena, R. Vignesh, G. Yasin, E. Hannachi, M. A. Almessiere, Z. Trabelsi, K.M. Batoo, A. Baykal, N. Sfina, Ceram. Int. 48 (20) (2022) 30499–30509.
[27] R.R. Kanna, K. Sakthipandi, N. Lenin, E.J.J. Samuel, J. Mater. Sci. Mater. Electron. 30 (2019) 4473–4486.
[28] R. Jasrotia, V.P. Singh, R. Kumar, R. Verma, A. Chauhan, Results Phys. 15 (2019) 102544.
[29] R.V. Bharathi, M.K. Raju, P.S.V. Shanmukhi, M.G. Kiran, N. Murali, D. Parajuli, T. W. Mammo, K. Samatha, Inorg. Chem. Commun. (2023) 111713.
[30] K. Chandramouli, B. Suryanarayana, P.P. Varma, V. Raghavendra, K.A. Emmanuel, P. Taddesse, N. Murali, T.W. Mammo, D. Parajuli, Results Phys. 24 (2021) 104117.
[31] K. Chandramouli, P.A. Rao, B. Suryanarayana, V. Raghavendra, S.J. Mercy, D. Parajuli, P. Taddesse, S.Y. Mulushoa, T.W. Mammo, N. Murali, J. Mater. Sci. Mater. Electron. 32 (12) (2021) 15754–15762.
[32] E. Ahilandeswari, R.R. Kanna, K. Sakthipandi, Physica B: Condensed Matter 599 (2020) 412425.
[33] K.L. Routray, S. Saha, D. Behera, Appl. Phys. A 125 (2019) 1–15.
[34] R. Rani, K.M. Batoo, P. Sharma, G. Anand, G. Kumar, S. Bhardwaj, M. Singh, Ceram. Int. 47 (21) (2021) 30902–30910.
[35] C. Rambabu, B. Arun, P.S.V. Shanmukhi, M.G. Kiran, N. Murali, T.W. Mammo, D. Parajuli, P. Choppara, P. Himakar, P.L. Narayana, Inorg. Chem. Commun., 2023, 111753.
[36] R.R. Kanna, K. Sakthipandi, A.S. Kumar, N.R. Dhineshbabu, S.S.M.A. Maraikkayar, A.S. Afroze, R.B. Jotania, M. Sivabharathy, Ceram. Int. 46 (9) (2020) 13695–13703.
[37] I.H. Gul, A. Maqsood, J. Alloy. Compd. 465 (1–2) (2008) 227–231.
[38] I.H. Gul, W. Ahmed, A. Maqsood, J. Magn. Magn. Mater. 320 (3–4) (2008) 270–275.
[39] I.H. Gul, F. Amin, A.Z. Abbasi, M. Anis-ur-Rehman, A. Maqsood, Scripta Comput. Sci. Appl. Math. Materialia 56 (6) (2007) 497–500.
[40] M.Z. Khan, I.H. Gul, A. Malik, J. Supercond. Nov. Magn. 33 (2020) 3133–3144.
[41] K. Sakthipandi, K. Kannagi, A. Hossain, Ceram. Int. 46 (11) (2020) 19634–19638.
[42] J. Guo, B. He, Y. Han, H. Liu, J. Han, X. Ma, J. Wang, W. Gao, W. Lü, Nano Lett. 24 (4) (2024) 1114–1121.
[43] Zhao, L., Fang, H., Wang, J., Nie, F., Li, R., Wang, Y. and Zheng, L., Applied Physics Letters, 124(3) 92024) 30501.
[44] S. Zhu, J. Zhu, S. Ye, K. Yang, M. Li, H. Wang, J. He, J. Am. Ceram. Soc. 106 (10) (2023) 6279–6291.
[45] S. Zhu, J. Zhu, S. Ye, Y. Zhang, S. Zhang, K. Yang, M. Li, H. Zou, H. Wang, J. He, Surf. Coat. Technol. 478 (2024) 130414.
[46] Y. Wang, J. Zhu, M. Li, G. Shao, H. Wang, R. Zhang, Mater. Des. 236 (2023) 112485.
[47] H. Wang, Z. Huang, X. Zeng, J. Li, Y. Zhang, Q. Hu, ACS Applied Electronic Materials 5 (7) (2023) 3726–3732.
[48] Z. Huang, Y. Zhang, H. Wang, J. Li, Appl. Phys. Lett. 123 (10) (2023) 103501.
[49] X. Long, K. Chong, Y. Su, L. Du, G. Zhang, Eng. Fract. Mech. 281 (2023) 109137.
[50] J. Wang, P. Wang, W. Chen, F. Wan, Y. Lu, Z. Tang, A. Dong, Z. Lei, Z. Zhang, Sens. Actuators B 380 (2023) 133350.
[51] Q. Zhu, J. Chen, G. Gou, H. Chen, P. Li, J. Mater. Process. Technol. 246 (2017) 267–275.
[52] X. Li, P. Yu, X. Niu, H. Yamaguchi, D. Li, J. Magn. Magn. Mater. 497 (2020) 165957.
[53] Z. Dong, X. Li, H. Yamaguchi, P. Yu, J. Magn. Magn. Mater. 589 (2024) 171501.
[54] G. Zhang, Z. Yang, X. Li, S. Deng, Y. Liu, H. Zhou, M. Peng, Z. Fu, R. Chen, D. Meng, L. Zhong, ACS Applied Electronic Materials 6 (2) (2024) 1339–1346.
[55] J. Zhang, X. Wang, L. Zhou, G. Liu, D.T. Adroja, I. da Silva, F. Demmel, D. Khalyavin, J. Sannigrahi, H.S. Nair, L. Duan, Adv. Mater. 34 (12) (2022) 2106728.
[56] N. Wang, X. Li, X. Lian, Q. Zhuang, J. Wang, J. Li, H. Qian, K. Miao, Y. Wang, X. Luo, G. Feng, Inorg. Chem. 63 (9) (2024) 4393–4403.
[57] Y. Su, Z. Shen, X. Long, C. Chen, L. Qi, X. Chao, Mater. Sci. Eng. A 872 (2023) 145001.
[58] K. Chandramouli, V. Raghavendra, P.P. Varma, B. Suryanarayana, T.W. Mammo, D. Parajuli, P. Taddesse, N. Murali, Appl. Phys. A 127 (2021) 1–14.